remote sensing

MDPI

Article

Hyperspectral Imaging of Adaxial and Abaxial Leaf Surfaces for Rapid Assessment of Foliar Nutrient Concentrations in Hass Avocado

Nimanie S. Hapuarachchi [1], Stephen J. Trueman [1], Wiebke Kämper [1,2], Michael B. Farrar [1], Helen M. Wallace [1], Joel Nichols [1] and Shahla Hosseini Bai [1,*]

[1] Centre for Planetary Health and Food Security, School of Environment and Science, Griffith University, Nathan, QLD 4111, Australia; nimanie.hapuarachchi@griffithuni.edu.au (N.S.H.); s.trueman@griffith.edu.au (S.J.T.); wiebke.kaemper@uni-goettingen.de (W.K.); m.farrar@griffith.edu.au (M.B.F.); helen.wallace@griffith.edu.au (H.M.W.); j.nichols2@griffith.edu.au (J.N.)

[2] Functional Agrobiodiversity, Department of Crop Sciences, University of Göttingen, 37077 Göttingen, Germany

* Correspondence: s.hosseini-bai@griffith.edu.au

Abstract: Rapid assessment tools are required for monitoring crop nutrient status and managing fertiliser applications in real time. Hyperspectral imaging has emerged as a promising assessment tool to manage crop nutrition. This study aimed to determine the potential of hyperspectral imaging for predicting foliar nutrient concentrations in avocado trees and establish whether imaging different sides of the leaves affects prediction accuracy. Hyperspectral images (400–1000 nm) were taken of both surfaces of leaves collected from Hass avocado trees 0, 6, 10 and 28 weeks after peak anthesis. Partial least squares regression (PLSR) models were developed to predict mineral nutrient concentrations using images from (a) abaxial surfaces, (b) adaxial surfaces and (c) combined images of both leaf surfaces. Modelling successfully predicted foliar nitrogen (R_P^2 = 0.60, RPD = 1.61), phosphorus (R_P^2 = 0.71, RPD = 1.90), aluminium (R_P^2 = 0.88, RPD = 2.91), boron (R_P^2 = 0.63, RPD = 1.67), calcium (R_P^2 = 0.88, RPD = 2.86), copper (R_P^2 = 0.86, RPD = 2.76), iron (R_P^2 = 0.81, RPD = 2.34), magnesium (R_P^2 = 0.87, RPD = 2.81), manganese (R_P^2 = 0.87, RPD = 2.76) and zinc (R_P^2 = 0.79, RPD = 2.21) concentrations from either the abaxial or adaxial surface. Foliar potassium concentrations were predicted successfully only from the adaxial surface (R_P^2 = 0.56, RPD = 1.54). Foliar sodium concentrations were predicted successfully (R_P^2 = 0.59, RPD = 1.58) only from the combined images of both surfaces. In conclusion, hyperspectral imaging showed great potential as a rapid assessment tool for monitoring the crop nutrition status of avocado trees, with adaxial surfaces being the most useful for predicting foliar nutrient concentrations.

Keywords: fertilisers; mineral nutrients; *Persea americana*; plant health; plant nutrition; visible near-infrared spectroscopy

check for updates

Citation: Hapuarachchi, N.S.; Trueman, S.J.; Kämper, W.; Farrar, M.B.; Wallace, H.M.; Nichols, J.; Bai, S.H. Hyperspectral Imaging of Adaxial and Abaxial Leaf Surfaces for Rapid Assessment of Foliar Nutrient Concentrations in Hass Avocado. *Remote Sens.* **2023**, *15*, 3100. https://doi.org/10.3390/rs15123100

Academic Editors: María Luisa Pérez-Bueno and Gregorio Egea

Received: 19 April 2023
Revised: 2 June 2023
Accepted: 12 June 2023
Published: 13 June 2023

1. Introduction

Tree crops contribute 600 million tons to global food production yearly, predominantly in the form of fruits and nuts [1–3]. Nutrient deficiencies in tree crops can result in low yield and poor fruit quality, and it is imperative to prevent these deficiencies through timely fertiliser applications [4–7]. Leaves are typically used to analyse crop nutrient status because foliar nutrient concentrations are often strong indicators of potential yield [8]. However, nutrient analyses are laborious and time-consuming, creating delays between foliar sampling and fertiliser application [8,9]. Rapid assessment technology is required to assess crop nutrition in real time, allowing for the timely scheduling of fertiliser amendments to sustain crop yield and quality [7,10].

Hyperspectral imaging (HSI) is emerging as a rapid quality assessment technique for tree crops [11–14]. Hyperspectral imaging integrates both digital imaging and spectroscopy to produce a spatial and spectral map of the target that cannot be obtained from traditional cameras [14–16]. Accuracies of HSI for predicting nut rancidity can be greater than using Red–Green–Blue (RGB), with R^2 of prediction being 93.48% and 39.13%, respectively [16]. Hyperspectral imaging can indirectly predict the external and internal composition of food products and detect defects or alterations that are not visible to the naked eye [14,16–21]. This rapid assessment technique has been successfully used in recent years to detect crop diseases, fruit and nut quality, and the concentrations of foliar biochemical compounds [17,22]. Hyperspectral imaging methods have been developed for predicting foliar nutrient concentrations in a variety of tree crops, including apple, cacao, citrus, macadamia and peach [23–27]. Mineral nutrients are bound to organic macromolecules that are essential for cell structure and function, and HSI has the ability to indirectly detect these mineral nutrients by detecting those organo-mineral bonds [28]. Hyperspectral imaging systems can be ground-based or mounted on unmanned aerial vehicles, both of which have been used to predict foliar nutrient concentrations because they can acquire high-resolution images [22,29,30]. Image collection from ground-based systems can be impacted by illumination effects and shadows [22]. On the other hand, drones have limited battery life, high operational complexity and requirements to comply with flight regulations [22,31]. The operational issues associated with unmanned aerial vehicles can be overcome by developing efficient and accessible laboratory-based imaging systems.

Laboratory-based imaging systems have become increasingly cost effective and they can provide real-time data on foliar nutrient concentrations [23–26]. Hyperspectral imaging has been used to predict nutrient concentrations by imaging either homogenised leaves or one surface of fresh leaves [24–26,29]. However, hyperspectral imaging of the adaxial (top) and abaxial (bottom) sides of leaves has rarely been compared for their capacity to predict nutrient concentrations. Differences in structure and chlorophyll concentrations exist between the adaxial and abaxial sides of citrus leaves, which can affect the prediction accuracies for foliar nutrient concentrations [23]. Hyperspectral image data from the adaxial surface of citrus and macadamia leaves have provided higher accuracy in predicting foliar nutrient concentrations than data collected from the abaxial surface, possibly because the adaxial side has a smoother wax layer and higher chlorophyll content than the abaxial side [23,27]. It is important to assess the prediction accuracy of images collected from the adaxial and abaxial sides of leaves to provide best practice for hyperspectral image collection.

Avocado is a tropical tree crop that produces fruit rich in unsaturated fatty acids, dietary fibre, micronutrients and vitamins [32,33]. Avocado production is increasing annually to meet the growing demand for healthy, nutrient-rich food [1]. However, avocado orchard productivity is often constrained by sub-optimal crop nutrient levels [34,35]. Nutrient levels within the avocado tree need to be sufficient to meet specific physiological demands during each stage of vegetative growth, flowering and fruit development [35]. Monitoring and maintaining nitrogen, phosphorus, potassium and boron concentrations during fruit set and development are critical to sustaining avocado yield [34–36]. Rapid assessment tools such as airborne laser scanning have been used to estimate the crown area, crown volume and tree count in avocado orchards [37], and HSI has been used to determine avocado fruit maturity and flesh nutrient concentrations [18,38]. However, HSI has not been used to assess avocado crop nutrient status and so further research is required to determine whether HSI can be used as a rapid assessment tool to detect foliar nutrient levels in avocado trees. Avocado leaves, like citrus leaves [23], have waxy cuticles and contain stomata only on their abaxial surface [34,39]. Therefore, the capacity to predict foliar nutrient concentrations might depend on which surface of the avocado leaf is used to capture hyperspectral images.

This study investigated the potential of laboratory-based HSI to predict the crop nutrition status of Hass avocado trees. The aim was to develop a tool for accurate and real-time assessment of the crop nutrient status, which would enable more efficient management of crop nutrition. Specifically, this study aimed to determine the accuracy of HSI in predicting foliar nutrient concentrations and the extent to which imaging of the two different sides of the leaf affects the prediction accuracy.

2. Materials and Methods

2.1. Sample Collection

Leaves were collected from 30 Hass trees located at the Eastridge avocado orchard (25°13′25″S 152°18′54″E), near Childers, Queensland, Australia. These trees were used in a previous complementary study on the effect of boron applications on avocado fruit set, yield and quality [36]. Four heterogeneous leaves were randomly collected from each experimental tree on each of four occasions: 0, 6, 10 and 28 weeks after peak flower anthesis. Each tree was divided into four quadrants, with one quadrant at each of the four cardinal directions around the tree. One young, fully expanded leaf was sampled per quadrant, at approximately 1.5 m from the ground, on each occasion.

2.2. Hyperspectral Imaging System, Image Acquisition and Spectral Data Extraction

Images of the leaves were captured in a laboratory setting using a visible/near-infrared HSI system. The system has a 12-bit push-broom line-scanning camera (Pika XC2, Resonon, Bozeman, MT, USA) with a spectral resolution of approximately ~1.3 nm, producing 462 wavelength bands between 400 nm and 1000 nm. The leaves were placed on a black background on the camera translation stage. The speed of the translation stage and exposure time were manually set to 1.23 mm s^{-1} and 19.7 ms, respectively. Image calibration and data extraction were carried out using SpectrononPro software (Version 2.96, Resonon, Bozeman, MT, USA). Image calibration was carried out prior to image acquisition via response correction (white calibration) and the removal of dark current noise (dark calibration). White calibration was obtained by capturing an image of a white Teflon sheet that reflected ≈99% of incident light. Dark calibration was carried out by capturing an image with the camera lens covered by its cap.

Images were acquired of both the abaxial and adaxial surfaces of the leaves, with each image containing four leaves from one tree at each time point, i.e., in total 30 images × 4 sampling time points per leaf surface were acquired. A region of interest (ROI) was marked on both the abaxial and adaxial surfaces (Figure 1). The mean raw reflectance (R_0) of the ROI was extracted and the mean corrected relative reference (R) was calculated using SpectrononPro software, using Equation (1):

$$R = (R_0 - D)/(W - D) \tag{1}$$

where D is the reflectance of an image captured with the lens covered and W is the reflectance of the white Teflon sheet.

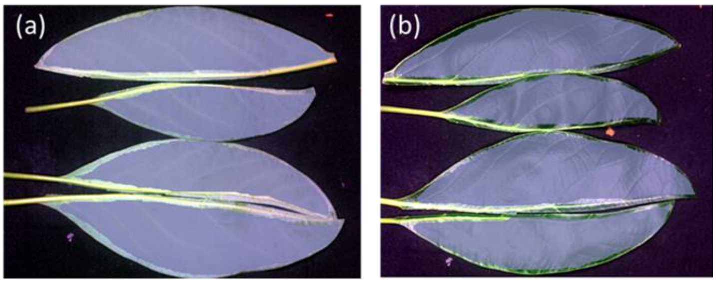

Figure 1. Selection of the regions of interest (denoted in grey colour) on the (**a**) abaxial and (**b**) adaxial surfaces of Hass avocado leaves.

2.3. Mineral Nutrient Analysis

The leaves were dried and ground after capturing the images. The four leaves from each tree at each sampling time were combined together as one sample. A subsample of at least 300 mg from each sample was used to analyse the concentrations of 13 nutrients.

The concentration of nitrogen (N) was determined by combustion analysis using a LECO CNS 928 analyser (TruSpec®, LECO Corporation, St. Joseph, MI, USA) [40,41]. Aluminium (Al), boron (B), calcium (Ca), copper (Cu), iron (Fe), magnesium (Mg), manganese (Mn), phosphorus (P), potassium (K), sodium (Na), sulphur (S) and zinc (Zn) concentrations were analysed via inductively coupled plasma–optical emission spectroscopy (Vista Pro®, Varian Incorporation, Palo Alto, CA, USA), after digestion with a 5:1 mixture of nitric and perchloric acids [42,43].

2.4. Calibration Model Development

The mean reflectance data from (a) 120 images of abaxial leaf surfaces, (b) 120 images of adaxial leaf surfaces and (c) combined images of both leaf surfaces (120 × 2 surfaces = 240 images) were used for subsequent model development. Following principal component analysis, Hotelling's T^2 test at a 95% confidence level was performed to identify spectral outliers within the samples [44]. The identified spectral outliers were removed and the remaining samples were divided randomly into two datasets, with approximately 80% and 20% of the samples being assigned to calibration sets and test sets, respectively [45]. Descriptive statistics for the calibration and test sets are provided (Table 1).

Table 1. Descriptive statistics for foliar mineral nutrient concentrations in Hass avocado using datasets of images from different leaf surfaces.

Variable	Surface	Calibration Set					Test Set				
		Mean	**SD**	**Min.**	**Max.**	**CV**	**Mean**	**SD**	**Min.**	**Max.**	**CV**
N	Abaxial	2.51	0.36	1.49	3.28	0.14	2.52	0.27	2.04	2.95	0.11
	Adaxial	2.54	0.34	1.48	3.28	0.13	2.41	0.34	1.83	3.04	0.14
	Combined	2.51	0.35	1.48	3.28	0.14	2.53	0.30	1.83	3.22	0.12
P	Abaxial	0.202	0.042	0.118	0.297	0.208	0.217	0.044	0.133	0.289	0.203
	Adaxial	0.204	0.042	0.118	0.284	0.206	0.208	0.048	0.128	0.297	0.231
	Combined	0.206	0.043	0.118	0.297	0.209	0.199	0.042	0.118	0.275	0.211
K	Abaxial	1.04	0.24	0.56	1.63	0.23	0.96	0.30	0.57	1.57	0.31
	Adaxial	1.03	0.26	0.56	1.63	0.25	1.05	0.27	0.70	1.49	0.26
	Combined	1.02	0.26	0.56	1.63	0.25	1.04	0.25	0.57	1.63	0.24
Al	Abaxial	52.1	46.0	13.1	180.9	0.9	53.8	49.0	15.4	168.6	0.9
	Adaxial	53.4	47.4	13.1	177.4	0.9	56.4	53.1	15.7	201.2	0.9
	Combined	56.4	49.4	13.1	201.2	0.9	45.8	44.3	13.1	177.4	1.0
B	Abaxial	70.0	35.3	24.3	188.1	0.5	69.1	28.4	28.2	155.8	0.4
	Adaxial	70.1	34.0	24.3	188.1	0.5	66.6	34.5	25.0	172.2	0.5
	Combined	69.4	33.3	24.3	188.1	0.5	68.4	37.3	25.0	188.1	0.6
Ca	Abaxial	0.932	0.483	0.300	2.28	0.5	0.840	0.309	0.268	1.62	0.4
	Adaxial	0.959	0.486	0.268	2.28	0.5	0.828	0.367	0.373	1.85	0.4
	Combined	0.925	0.456	0.268	2.28	0.5	0.928	0.481	0.358	1.85	0.5
Cu	Abaxial	55.3	44.6	10.0	160.4	0.8	56.5	45.2	10.6	123.6	0.8
	Adaxial	57.0	45.5	10.0	160.4	0.8	44.7	39.8	10.5	121.8	0.9
	Combined	57.1	44.7	10.0	160.4	0.8	47.2	42.7	10.3	144.8	0.9
Fe	Abaxial	92.7	50.4	40.5	270.9	0.5	99.2	60.4	43.0	252.8	0.6
	Adaxial	93.6	51.4	42.6	252.8	0.6	104.1	58.3	40.5	270.9	0.6
	Combined	96.7	66.0	40.5	681.6	0.7	112.9	103.8	42.6	681.6	0.9
Mg	Abaxial	0.280	0.117	0.129	0.631	0.4	0.286	0.119	0.133	0.495	0.4
	Adaxial	0.287	0.121	0.129	0.631	0.4	0.279	0.112	0.157	0.524	0.4
	Combined	0.281	0.117	0.129	0.631	0.4	0.298	0.121	0.129	0.611	0.4
Mn	Abaxial	926	615	276	2558	0.7	926	530	383	2118	0.6
	Adaxial	953	603	276	2697	0.6	965	693	299	2558	0.7
	Combined	933	592	276	2697	0.6	1005	706	276	2508	0.7
Na	Abaxial	113.0	47.6	40.1	272.6	0.4	115.6	42.1	39.5	207.1	0.4
	Adaxial	114.9	48.4	39.5	272.6	0.4	108.1	36.8	51.5	195.2	0.3
	Combined	116.3	51.7	39.5	345.9	0.4	110.7	46.3	50.2	345.9	0.4

Table 1. *Cont.*

Variable	Surface	Calibration Set					Test Set				
		Mean	**SD**	**Min.**	**Max.**	**CV**	**Mean**	**SD**	**Min.**	**Max.**	**CV**
S	Abaxial	2373	443	1329	3510	0.2	2416	497	1741	3340	0.2
	Adaxial	2379	456	1329	3510	0.2	2461	405	1749	3340	0.2
	Combined	2397	461	1329	3954	0.2	2422	513	1538	3954	0.2
Zn	Abaxial	39.3	8.4	24.3	59.3	0.2	40.5	8.3	28.4	55.6	0.2
	Adaxial	39.0	8.2	24.3	57.5	0.2	41.8	8.0	30.8	59.3	0.2
	Combined	40.0	8.7	24.3	76.8	0.2	38.7	9.7	26.7	76.8	0.3

Nutrient concentrations are expressed in mg/kg, except N (nitrogen), P (phosphorus), K (potassium), Ca (calcium) and Mg (magnesium) concentrations, which are expressed as %. SD: standard deviation; CV: coefficient of variation. The means of the calibration and test sets within a row did not differ significantly (Student's *t*-test; $p < 0.05$).

The calibration and test sets were tested for homogeneity of variance, and Student's *t*-test was performed to identify differences between the means. A variety of spectral data transformations was explored using the calibration datasets to remove scatter effects and random noise [46,47]. The spectral data transformations explored included multiplicative scatter correction (MSC), orthogonal signal correction (OSC), standard normal variate (SNV) and detrending [46,48].

Partial least squares regression (PLSR) models were then developed using both raw and transformed spectral data to establish correlations between foliar mineral nutrient concentrations and mean reflectance data in the 400–1000 nm spectral range. PLSR is the preferred method for analysing data with numerous highly correlated independent variables and few response variables [47,49]. A full cross-validation (leave-one-out) method was used during model development to select the optimal number of components and avoid over-fitting and, therefore, obtain a model with optimum performance [50].

2.5. Model Evaluation

The models were assessed by selection of the highest coefficient of determination for calibration (R^2_C) and cross-validation (R^2_V), and the lowest root mean square error for calibration ($RMSE_C$) and cross-validation ($RMSE_V$). The R^2 and RMSE are defined by Equations (2) and (3):

$$R^2 = 1 - \frac{\Sigma_{i=1}^{n}\left(y_i - \hat{y}_i\right)^2}{\Sigma_{i=1}^{n}\left(y_i - \bar{y}\right)^2} \tag{2}$$

$$RMSE = \sqrt{\left(\Sigma_{i=1}^{n}\left(\hat{y}_i - y_i\right)^2\right)/n} \tag{3}$$

where y_i and $\hat{y}_i$ are the reference and predicted values in the ith sample, $\bar{y}$ is the mean of the reference values and n was the number of samples. Finally, the prediction ability of all calibration models was assessed using the test set.

The prediction capacity of the calibration models was evaluated using the coefficient of determination (R^2_P), root mean square error ($RMSE_P$) and the ratio of prediction-to-deviation (RPD) of the test set [51]. The RPD was calculated using Equation (4):

$$RPD = SD_P/RMSE_P \tag{4}$$

where SD_P is the standard deviation of the reference values in the test set [44,52]. Robustness was evaluated by assessing the RPD of the model calculated using the test set [52]. Models with an RPD > 2.0 are considered highly reliable with excellent prediction capacity, while models with an RPD from 1.4 to 2.0 are considered reliable with good prediction capacity [53]. PLSR regression coefficients (i.e., β-coefficients) are also used to provide information about the importance of each wavelength in the developed model [13,47].

The predicted concentrations for each nutrient from the leaf images were calculated using Equation (5):

$$\widehat{Y} = b_0 + b_1x_1 + b_2x_2 + \cdots + b_kx_k \quad (5)$$

where $\widehat{Y}$ is the predicted response value, x_1, x_2, ..., x_k are the predictor values at each wavelength, and b_0, b_1, b_2, ..., b_k are the regression coefficients at each wavelength [54]. Descriptive analysis of the calibration and test sets, outlier detection, spectral data transformations and PLSR model development were carried out using Unscrambler software (Version 10.5.1, CAMO, Trondheim, Norway).

3. Results

3.1. Descriptive Analysis of Foliar Nutrient Concentrations in the Calibration and Test Sets

The mean concentrations for each foliar nutrient were within the same ranges in the calibration and test sets of each image dataset (abaxial, adaxial and combined surfaces) (Table 1).

3.2. Reflectance of Leaf Images

The mean reflectance of the abaxial surface differed from that of the adaxial surface at wavelengths between 500 and 700 nm, and between 750 and 1000 nm (Figure 2). The abaxial surface gave the highest mean reflectance between 500 and 700 nm, whereas the adaxial surface gave highest mean reflectance between 750 and 1000 nm (Figure 2).

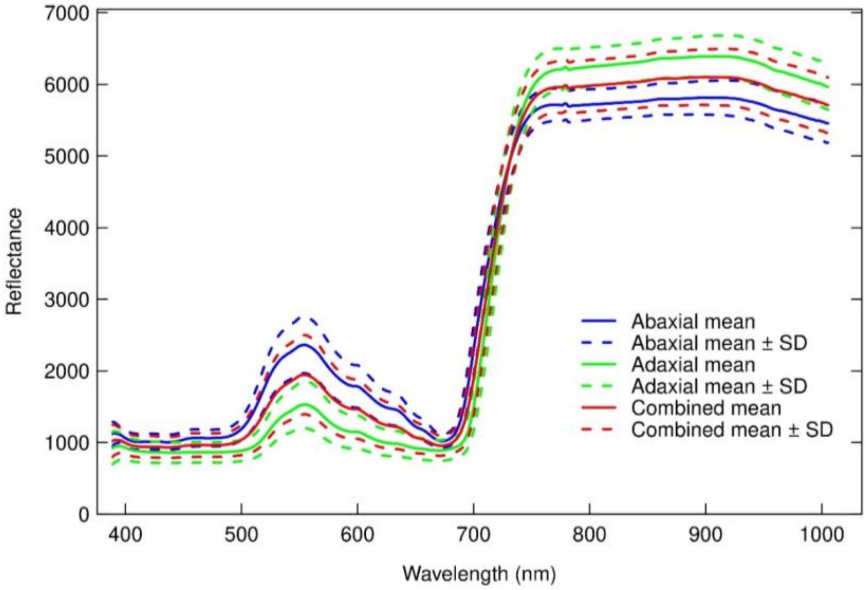

Figure 2. Mean (± SD) relative reflectance of the Vis/NIR spectrum (400–1000 nm) extracted from abaxial (n = 120), adaxial (n = 120) and combined surfaces (n = 240) of Hass avocado leaves.

3.3. Prediction Performance

PLSR models were developed that predicted foliar concentrations of N, P, K, Al, B, Ca, Cu, Fe, Mg, Mn, Na and Zn, with RPDs between 1.43 and 2.91. The best-fit PLSR models for predicting foliar N, P, K, B and Na concentrations had RPDs between 1.54 and 1.90 (Table 2). The best-fit PLSR models for predicting foliar Al, Ca, Cu, Fe, Mg, Mn and Zn concentrations had RPDs > 2.00 (Table 2). A reliable model to predict foliar S concentration was not able to be developed because the models developed using images of abaxial, adaxial or combined surfaces all had RPDs < 1.00 (Table 2).

Table 2. Performance of PLSR models in predicting foliar mineral nutrient concentrations in Hass avocado leaves using datasets from hyperspectral images of abaxial, adaxial or combined leaf surfaces.

Variable	**Image**	**Transformation**	**LV**	**Calibration Set**		**Validation Set**		**Test Set**		
				RMSE$_C$	**R^2$_C$**	**RMSE$_V$**	**R^2$_V$**	**RMSE$_P$**	**R^2$_P$**	**RPD**
N	Abaxial	–	10	0.20	0.67	0.25	0.52	0.17	0.60	1.61
	Adaxial	SNV	4	0.22	0.57	0.24	0.50	0.24	0.49	1.43
	Combined	–	15	0.19	0.72	0.22	0.61	0.22	0.45	1.55
P	Abaxial	–	6	0.02	0.67	0.03	0.58	0.02	0.71	1.90
	Adaxial	MSC	5	0.02	0.71	0.03	0.64	0.03	0.63	1.67
	Combined	–	7	0.03	0.66	0.03	0.63	0.03	0.58	1.04
K	Abaxial	–	9	0.15	0.60	0.18	0.44	0.22	0.43	1.36
	Adaxial	OSC	2	0.15	0.66	0.17	0.58	0.18	0.56	1.54
	Combined	Detrend	9	0.17	0.55	0.19	0.46	0.19	0.43	0.92
Al	Abaxial	Detrend	5	16.8	0.87	18.5	0.84	16.8	0.88	2.91
	Adaxial	SNV	4	16.8	0.87	18.1	0.86	22.2	0.82	2.39
	Combined	–	7	17.1	0.88	18.2	0.86	16.6	0.86	2.67
B	Abaxial	MSC	5	22.8	0.58	25.5	0.48	19.5	0.51	1.46
	Adaxial	MSC	4	23.3	0.53	25.4	0.45	20.7	0.63	1.67
	Combined	SNV	5	29.5	0.48	31.5	0.41	28.5	0.40	1.31
Ca	Abaxial	–	5	0.18	0.86	0.20	0.83	0.19	0.59	1.59
	Adaxial	MSC + Detrend	4	0.21	0.82	0.22	0.79	0.23	0.58	1.58
	Combined	–	6	0.22	0.76	0.23	0.75	0.17	0.88	2.86
Cu	Abaxial	–	3	19.3	0.81	20.2	0.80	16.4	0.86	2.76
	Adaxial	OSC	1	17.1	0.86	17.4	0.86	14.7	0.86	2.71
	Combined	SNV	3	19.9	0.80	20.4	0.79	20.4	0.77	2.09
Fe	Abaxial	–	4	28.2	0.68	30.9	0.63	25.8	0.81	2.34
	Adaxial	SNV	4	26.9	0.72	29.2	0.68	29.8	0.73	1.96
	Combined	–	6	26.1	0.73	27.4	0.71	34.7	0.67	1.75
Mg	Abaxial	OSC	2	0.04	0.89	0.04	0.88	0.04	0.87	2.81
	Adaxial	MSC	4	0.05	0.83	0.06	0.80	0.04	0.85	2.68
	Combined	MSC	6	0.05	0.83	0.05	0.81	0.04	0.87	2.80
Mn	Abaxial	MSC	3	228	0.86	245	0.84	246	0.85	2.15
	Adaxial	MSC	4	274	0.79	297	0.76	273	0.84	2.54
	Combined	MSC	5	273	0.79	289	0.76	256	0.87	2.76
Na	Abaxial	MSC	4	35.7	0.43	39.6	0.32	34.5	0.30	1.22
	Adaxial	–	3	40.2	0.31	42.7	0.23	31.1	0.25	1.18
	Combined	SNV	11	37.1	0.48	43.0	0.31	29.3	0.59	1.58
S	Abaxial	–	4	341	0.40	369	0.31	545	NA	0.91
	Adaxial	SNV	4	377	0.31	411	0.20	377	0.09	1.07
	Combined	–	3	410	0.20	421	0.17	489	0.09	1.05
Zn	Abaxial	–	5	4.81	0.67	5.26	0.61	3.75	0.79	2.21
	Adaxial	SNV	5	4.50	0.69	4.98	0.63	5.62	0.49	1.43
	Combined	–	6	5.45	0.61	5.70	0.57	5.87	0.63	1.66

Nutrient concentrations are expressed in mg/kg, except N (nitrogen), P (phosphorus), K (potassium), Ca (calcium) and Mg (magnesium) concentrations, which are expressed as %. LV: number of latent variables; SNV: standard normal variate; MSC: multiplicative scatter correction; OSC: orthogonal signal correction.

The best-fit PLSR models for predicting foliar concentrations of N (RPD = 1.61), P (RPD = 1.90), Al (RPD = 2.91), Cu (RPD = 2.76), Fe (RPD = 2.34), Mg (RPD = 2.81) and Zn (RPD = 2.21) used data acquired from images of the abaxial surface (Table 2, Figures 3 and 4). Foliar N, Al, Cu, Fe, Mg and Zn concentrations were also predicted successfully from adaxial and combined surface images, which provided RPDs between 1.43 and 2.80 (Table 2). Foliar P concentration (RPD = 1.67) was also predicted successfully from images of the adaxial surface, but not the combined surface images (Table 2).

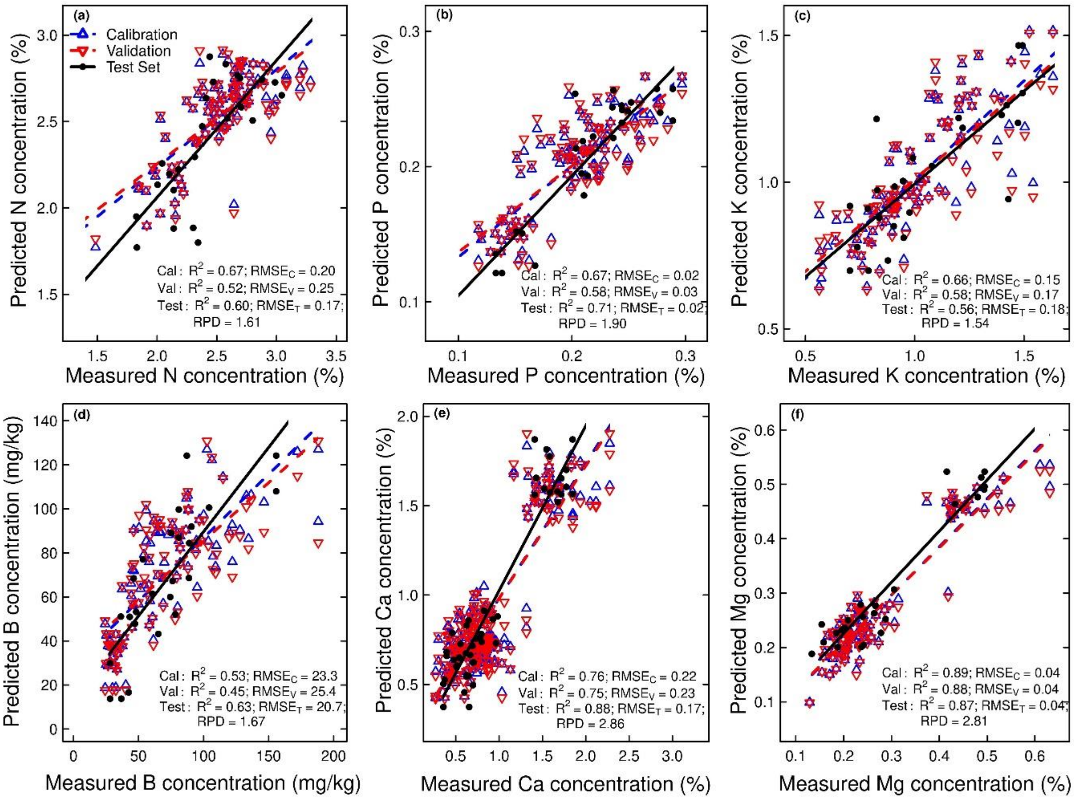

Figure 3. Measured vs. predicted concentrations of foliar (**a**) nitrogen, (**b**) phosphorus, (**c**) potassium, (**d**) boron, (**e**) calcium and (**f**) magnesium using the best-fit models from images of Hass avocado leaves.

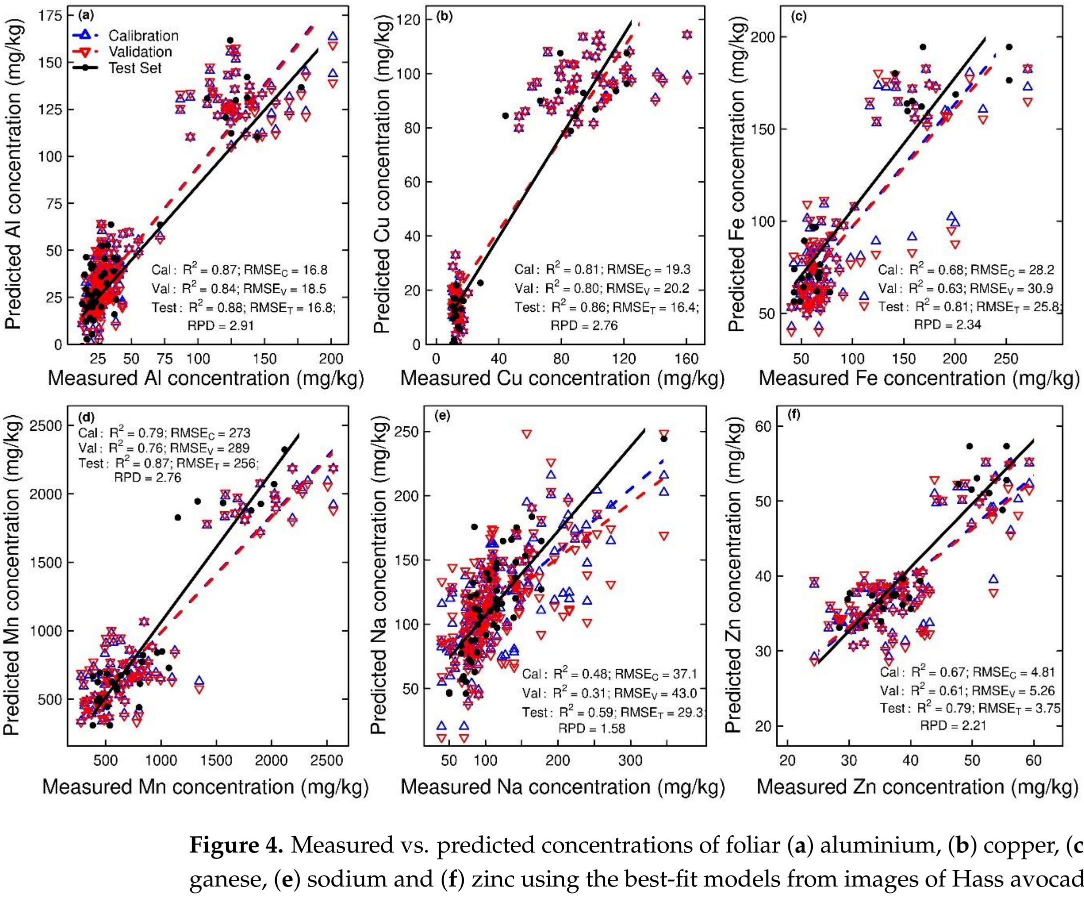

Figure 4. Measured vs. predicted concentrations of foliar (**a**) aluminium, (**b**) copper, (**c**) iron, (**d**) manganese, (**e**) sodium and (**f**) zinc using the best-fit models from images of Hass avocado leaves.

The best-fit PLSR models for predicting foliar concentrations of K (RPD = 1.54) and B (RPD = 1.67) used data acquired from the adaxial surface (Table 2 and Figure 3). The concentration of B (RPD = 1.46) could also be predicted from images of the abaxial surface (Table 2). The best-fit PLSR models for predicting foliar concentrations of Ca (RPD = 2.86), Mn (RPD = 2.76) and Na (RPD = 1.58) used combined surface images (Table 2, Figures 3 and 4). Foliar Ca and Mn concentrations could also be predicted successfully using images of the abaxial or adaxial surfaces, which provided RPDs between 1.58 and 2.54 (Table 2).

The β-coefficients indicated that the most important wavelengths for predicting foliar N, Al, Cu, Fe, Mg, Mn and Na concentrations were in both the visible and near-infrared regions (Figures S1–S4). The most important wavelengths for predicting foliar P, B and Zn concentrations were between 500 and 700 nm in the visible region, and for predicting foliar K and Ca concentrations between 700 and 1000 nm in the near-infrared region (Figures S1, S2 and S4).

4. Discussion

Hyperspectral imaging successfully predicted the concentrations of most nutrients in Hass avocado leaves. The best-fit PLSR models for predicting foliar Al, Ca, Cu, Fe, Mg, Mn and Zn concentrations provided excellent predictions, with RPDs between 2.21 and 2.91. The best-fit PLSR models for predicting foliar N, P, K, B and Na concentrations provided good predictions, with RPDs between 1.43 and 1.90. Foliar N, P, Al, B, Ca, Cu, Fe, Mg, Mn and Zn concentrations could be predicted from images of either the abaxial or adaxial surface. The foliar K concentration was only predicted successfully from images of the adaxial surface, and the foliar Na concentration was only predicted successfully using the combined surface images.

Model robustness was assessed using RPDs of the predicted nutrient concentrations in the test set, with an RPD > 2.0 considered highly reliable with excellent prediction capacity, and an RPD between 1.4 and 2.0 considered reliable with good prediction capacity [53]. The best-fit PLSR models for predicting foliar Al, Ca, Cu, Fe, Mg, Mn and Zn concentrations provided excellent predictions, as the RPDs were greater than 2.0. The best-fit PLSR models for predicting foliar N, P, K, B and Na concentrations provided good predictions, as the RPDs were between 1.4 and 2.0. High RPD values from the Al, Ca, Cu, Fe, Mg, Mn and Zn models could be associated partly with their wide and uneven data distributions, which were each separated into two distinct clusters with low and high concentrations. Nutrient demands by the crop and fertiliser applications across the period of flowering and fruit development could have caused these distinct clusters in the data for some nutrient concentrations. The leaf samples collected during flowering had significantly higher Al, Ca, Fe, Mg and Mn concentrations, and lower foliar Cu and Zn concentrations than those collected during fruit development. Foliar Ca, Fe, Mg and Mn concentrations are lowest during fruit development due to the nutrient demand from developing fruit [55–57]. The foliar Cu concentration can be low during flowering due to Cu demand by flowers [55,57].

Hyperspectral imaging could not predict foliar S concentrations using PLSR modelling. PLSR is commonly applied to datasets with a small number of samples [18,27,58–60], and foliar S concentrations have been predicted using PLSR models previously [18,27]. Therefore, the small number of samples in the dataset may not be directly associated with the lack of prediction capacity for foliar S concentrations. PLSR is appropriate when a linear relationship exists between spectral data and the variable of interest [59,60]. Other advanced machine learning methods such as artificial neural network (ANN) could be applied to increase the prediction capacity of the models [30,61]. ANN models provide high prediction accuracy when data are noisy and a nonlinear relationship exists between spectral data and the variable of interest [62]. However, ANN models are usually developed when a dataset has a large number of samples [61].

The most important wavelengths for predicting many of the nutrient concentrations were in both the visible and near-infrared regions. However, the most important wavelengths for predicting K and Ca concentrations were in the near-infrared region. Mineral nutrients can occur in plants in either organic or inorganic forms, often being bound in organic complexes [63]. Hyperspectral imaging detects mineral nutrients indirectly in the visible and near-infrared regions by detecting these organic complexes [63–66]. Reflectance in the visible region (400–700 nm) may be associated with pigment molecules such as chlorophyll, and reflectance in the near-infrared region (700–1000 nm) may be associated with protein, fatty acid and starch molecules [67–69]. The most important wavelengths for predicting the N concentration were found in the 400–500 nm, 520–680 nm, 700–820 nm and 850–1000 nm regions. Nitrogen is detected in both the visible and near-infrared regions because it is present as a component of both chlorophyll and proteins [24,58,63,68]. Potassium occurs in plants in an inorganic form and can be detected at 730–1000 nm when it forms complexes with carbohydrates such as starch and cellulose [24,63]. Calcium exists in plants as calcium pectate, a major component of cell walls, and this compound reflects at 710–730 nm, 770–820 nm and 860–1000 nm [24,63].

Hyperspectral imaging could predict most foliar nutrient concentrations from images of either the adaxial or abaxial leaf surface. The stability of the spectral reflectance data from an image is essential for high prediction accuracy, and the structural uniformity of the leaf surface contributes to the stability of spectral data [23]. Hyperspectral imaging of the adaxial surface is more suitable than imaging of the abaxial surface in predicting N and P concentrations in citrus leaves [23]. The adaxial side of citrus leaves has a continuous wax layer and is smoother, with a higher chlorophyll content than the abaxial side [23]. The adaxial surface of avocado leaves also has a continuous, thick, waxy cuticle and no stomata, while the abaxial surface has stomata and non-continuous wax deposits [34,39,70,71]. The adaxial side has a high chlorophyll content and dark green colour, while the abaxial side has a low chlorophyll content and light green colour [72,73]. However, the abaxial surface of Hass leaves is smoother than that of other avocado cultivars [39], which could explain why abaxial surface images were often also suitable for predicting many nutrient concentrations in Hass leaves. The capacity to predict most nutrient concentrations using images of one leaf surface, most commonly the adaxial surface, will assist in using hyperspectral imaging as a highly efficient, rapid assessment technique because the leaves will not need to be rotated to capture images of both surfaces.

The concentrations of essential nutrients for avocado productivity, such as N, P, K, B, Ca, Mg and Zn, were successfully predicted from the PLSR models. Deficiencies of N, P, K, Ca, Mg and Zn in avocado trees can induce alternate bearing, reduce yield, and cause fruit flesh disorders and body rots [34,35,74–77]. Nutrient toxicities in avocado can also occur due to the excessive use of fertiliser. For example, B is a critical nutrient for avocado fruit set and yield, but high B concentrations can cause fruitlet abscission and reduce yield [36]. Rapid nutrient assessment tools such as hyperspectral imaging could help growers detect nutrient deficiencies or toxicities in crops in real time, reduce fertiliser costs and manage nutrient applications more efficiently.

5. Conclusions

Hyperspectral imaging of either the abaxial or adaxial leaf surface showed great potential for the rapid assessment of foliar nutrient levels in Hass avocado trees. The predictive ability of these models should be validated for less commonly grown avocado cultivars, and further investigations are required into the use of field-based HSI systems to predict crop nutrient levels in avocado orchards. This technology could be used to diagnose nutrient deficiencies or toxicities in real time, allowing for an immediate re-scheduling of nutrient amendments and preventing the excessive use of fertilisers. Hyperspectral imaging and optimised fertiliser applications have the capacity to reduce fertiliser costs, increase fruit production, improve fruit quality and minimise nutrient runoff to the environment.

Supplementary Materials: The following supporting information can be downloaded at: https://www.mdpi.com/article/10.3390/rs15123100/s1, Figure S1: β-coefficients associated with the best-fit PLSR models for predicting (a) nitrogen, (b) phosphorus and (c) potassium concentrations in Hass avocado leaves; Figure S2: β-coefficients associated with the best-fit PLSR models for predicting (a) boron, (b) calcium and (c) magnesium concentrations in Hass avocado leaves; Figure S3: β-coefficients associated with the best-fit PLSR models for predicting (a) aluminium, (b) copper and (c) iron concentrations in Hass avocado leaves; Figure S4: β-coefficients associated with the best-fit PLSR models for predicting (a) manganese, (b) sodium and (c) zinc concentrations in Hass avocado leaves; Figure S5: Measured vs. predicted concentrations of foliar (a) aluminium, (b) calcium, (c) copper and (d) iron from Hass avocado leaves 0, 6, 10 and 28 weeks after peak anthesis; Figure S6: Measured vs. predicted concentrations of foliar (a) magnesium, (b) manganese and (c) zinc from Hass avocado leaves 0, 6, 10 and 28 weeks after peak anthesis; Table S1: Mineral nutrient concentrations in leaves 0, 6, 10 and 28 weeks after peak anthesis of Hass avocado trees.

Author Contributions: Conceptualization, S.H.B., S.J.T., H.M.W., W.K. and N.S.H.; methodology, S.H.B., S.J.T., W.K. and N.S.H.; investigation, N.S.H. and J.N.; formal analysis, N.S.H., S.H.B. and S.J.T.; data curation, N.S.H.; writing—original draft preparation, N.S.H.; writing—review and editing, S.H.B., S.J.T., H.M.W., W.K., M.B.F. and J.N.; supervision, S.H.B., S.J.T., H.M.W. and W.K.; funding acquisition, S.J.T., H.M.W. and S.H.B. All authors have read and agreed to the published version of the manuscript.

Funding: This study was funded by project PH16001 of the Hort Frontiers Pollination Fund, part of the Hort Frontiers strategic partnership initiative developed by Hort Innovation, with co-investment from Griffith University, University of the Sunshine Coast, Plant & Food Research Ltd. and contributions from the Australian Government. Nimanie Hapuarachchi was supported by the Griffith University International Postgraduate Research Scholarship and Griffith University Postgraduate Research Scholarship.

Data Availability Statement: The data presented in this study are available on request from the corresponding author.

Acknowledgments: The authors would like to thank Costa Avocado for assistance and access to the orchard, and Anushika De Silva, Sascha Kämper, Tsvakai Gama and David Appleton for assistance in the laboratory and fieldwork.

Conflicts of Interest: The authors declare that they have no known competing financial interests or personal relationships that could have appeared to influence the work reported in this paper.

References

1. FAO (Food and Agriculture Organisation). *Major Tropical Fruits—Preliminary Market Results 2021*; FAO: Rome, Italy, 2022.
2. Grünwald, N.J. Entering the international year of fruits and vegetables: Tradeoffs between food production and the environment. *CABI Agric. Biosci.* **2021**, *2*, 2. [CrossRef] [PubMed]
3. INDFC (International Nut and Dried Fruit Council). *Nuts and Dried Fruits Statistical Yearbook 2021/22*; INDFC: Reus, Spain, 2022.
4. Brunetto, G.; Melo, G.W.B.D.; Toselli, M.; Quartieri, M.; Tagliavini, M. The role of mineral nutrition on yields and fruit quality in grapevine, pear and apple. *Rev. Bras. Frutic.* **2015**, *37*, 1089–1104. [CrossRef]
5. Wang, Z.H.; Li, S.X.; Malhi, S. Effects of fertilization and other agronomic measures on nutritional quality of crops. *J. Sci. Food Agric.* **2008**, *88*, 7–23. [CrossRef]
6. Kumar, R.; Kumar, V. Physiological disorders in perennial woody tropical and subtropical fruit crops: A review. *Indian J. Agric. Sci.* **2016**, *86*, 703–717.
7. Lemaire, G.; Tang, L.; Bélanger, G.; Zhu, Y.; Jeuffroy, M.H. Forward new paradigms for crop mineral nutrition and fertilization towards sustainable agriculture. *Eur. J. Agron.* **2021**, *125*, 126248. [CrossRef]
8. Prado, R.M.; Rozane, D.E. Leaf analysis as diagnostic tool for balanced fertilization in tropical fruits. In *Fruit Crops: Diagnosis and Management of Nutrient Constraints*; Srivastava, A.K., Hu, C., Eds.; Elsevier: Amsterdam, The Netherlands, 2020; pp. 131–141.
9. Dimkpa, C.; Bindraban, P.S.; McLean, J.; Gatere, L.; Singh, U.; Hellums, D. Methods for rapid testing of plant and soil nutrients. In *Sustainable Agriculture Reviews*; Lichtfouse, E., Ed.; Springer: New York, NY, USA, 2017; Volume 25, pp. 1–43.
10. Barbedo, J.G.A. Detection of nutrition deficiencies in plants using proximal images and machine learning: A review. *Comput. Electron. Agric.* **2019**, *162*, 482–492. [CrossRef]
11. Wang, N.N.; Sun, D.W.; Yang, Y.C.; Pu, H.; Zhu, Z. Recent advances in the application of hyperspectral imaging for evaluating fruit quality. *Food Anal. Methods* **2016**, *9*, 178–191. [CrossRef]
12. Gama, T.; Wallace, H.M.; Trueman, S.J.; Tahmasbian, I.; Bai, S.H. Hyperspectral imaging for non-destructive prediction of total nitrogen concentration in almond kernels. *Acta Hortic.* **2018**, *1219*, 259–264. [CrossRef]

13. Bai, S.H.; Tahmasbian, I.; Zhou, J.; Nevenimo, T.; Hannet, G.; Walton, D.; Randall, B.; Gama, T.; Wallace, H.M. A non-destructive determination of peroxide values, total nitrogen and mineral nutrients in an edible tree nut using hyperspectral imaging. *Comput. Electron. Agric.* **2018**, *151*, 492–500. [CrossRef]
14. Li, X.; Li, R.; Wang, M.; Liu, Y.; Zhang, B.; Zhou, J. Hyperspectral imaging and their applications in the nondestructive quality assessment of fruits and vegetables. In *Hyperspectral Imaging in Agriculture, Food and Environment*; Maldonado, A.I.L., Rodriguez-Fuentes, H., Contreras, J.A.V., Eds.; Intech Open: London, UK, 2018; pp. 28–53.
15. Manley, M. Near-infrared spectroscopy and hyperspectral imaging: Non-destructive analysis of biological materials. *Chem. Soc. Rev.* **2014**, *43*, 8200–8214. [CrossRef] [PubMed]
16. Han, Y.; Liu, Z.; Khoshelham, K.; Bai, S.H. Quality estimation of nuts using deep learning classification of hyperspectral imagery. *Comput. Electron. Agric.* **2021**, *180*, 105868. [CrossRef]
17. Mishra, P.; Asaari, M.S.M.; Herrero-Langreo, A.; Lohumi, S.; Diezma, B.; Scheunders, P. Close range hyperspectral imaging of plants: A review. *Biosyst. Eng.* **2017**, *164*, 49–67. [CrossRef]
18. Kämper, W.; Trueman, S.J.; Tahmasbian, I.; Bai, S.H. Rapid determination of nutrient concentrations in Hass avocado fruit by Vis/NIR hyperspectral imaging of flesh or skin. *Remote Sens.* **2020**, *12*, 3409. [CrossRef]
19. Tahmasbian, I.; Wallace, H.M.; Gama, T.; Bai, S.H. An automated non-destructive prediction of peroxide value and free fatty acid level in mixed nut samples. *LWT-Food Sci. Technol.* **2021**, *143*, 110893. [CrossRef]
20. Han, Y.; Bai, S.H.; Trueman, S.J.; Khoshelham, K.; Kämper, W. Predicting the ripening time of 'Hass' and 'Shepard' avocado fruit by hyperspectral imaging. *Precis. Agric.* **2023**. [CrossRef]
21. Davur, Y.J.; Kämper, W.; Khoshelham, K.; Trueman, S.J.; Bai, S.H. Estimating the ripeness of Hass avocado fruit using deep learning with hyperspectral imaging. *Horticulturae* **2023**, *9*, 599. [CrossRef]
22. Lu, B.; Dao, P.D.; Liu, J.; He, Y.; Shang, J. Recent advances of hyperspectral imaging technology and applications in agriculture. *Remote Sens.* **2020**, *12*, 2659. [CrossRef]
23. Liu, Y.; Lyu, Q.; He, S.; Yi, S.; Liu, X.; Xie, R.; Zheng, Y.; Deng, L. Prediction of nitrogen and phosphorus contents in citrus leaves based on hyperspectral imaging. *Int. J. Agric. Biol. Eng.* **2015**, *8*, 80–88. [CrossRef]
24. Malmir, M.; Tahmasbian, I.; Xu, Z.; Farrar, M.B.; Bai, S.H. Prediction of macronutrients in plant leaves using chemometric analysis and wavelength selection. *J. Soils Sediments* **2020**, *20*, 249–259. [CrossRef]
25. Ye, X.; Abe, S.; Zhang, S. Estimation and mapping of nitrogen content in apple trees at leaf and canopy levels using hyperspectral imaging. *Precis. Agric.* **2020**, *21*, 198–225. [CrossRef]
26. Abenina, M.I.A.; Maja, J.M.; Cutulle, M.; Melgar, J.C.; Liu, H. Prediction of potassium in peach leaves using hyperspectral imaging and multivariate analysis. *AgriEngineering* **2022**, *4*, 400–413. [CrossRef]
27. De Silva, A.L.; Trueman, S.J.; Kämper, W.; Wallace, H.M.; Nichols, J.; Bai, S.H. Hyperspectral imaging of adaxial and abaxial leaf surfaces as a predictor of macadamia crop nutrition. *Plants* **2023**, *12*, 558. [CrossRef]
28. Wang, Y.J.; Jin, G.; Li, L.Q.; Liu, Y.; Kalkhajeh, Y.K.; Ning, J.M.; Zhang, Z.Z. NIR hyperspectral imaging coupled with chemometrics for nondestructive assessment of phosphorus and potassium contents in tea leaves. *Infrared Phys. Technol.* **2020**, *108*, 103365. [CrossRef]
29. Vigneau, N.; Ecarnot, M.; Rabatel, G.; Roumet, P. Potential of field hyperspectral imaging as a non destructive method to assess leaf nitrogen content in Wheat. *Field Crops Res.* **2011**, *122*, 25–31. [CrossRef]
30. Grieco, M.; Schmidt, M.; Warnemünde, S.; Backhaus, A.; Klück, H.C.; Garibay, A.; Tandrón Moya, Y.A.; Jozefowicz, A.M.; Mock, H.P.; Seiffert, U.; et al. Dynamics and genetic regulation of leaf nutrient concentration in barley based on hyperspectral imaging and machine learning. *Plant Sci.* **2022**, *315*, 111123. [CrossRef]
31. CASA (Civil Aviation Safety Authority). Remote Pilot License. Available online: https://www.casa.gov.au/drones/remote-pilot-licence (accessed on 14 March 2023).
32. Dreher, M.L.; Davenport, A.J. Hass avocado composition and potential health effects. *Crit. Rev. Food Sci. Nutr.* **2013**, *53*, 738–750. [CrossRef]
33. Dreher, M.L.; Cheng, F.W.; Ford, N.A. A comprehensive review of Hass avocado clinical trials, observational studies, and biological mechanisms. *Nutrients* **2021**, *13*, 4376. [CrossRef]
34. Lahav, E.; Whiley, A.W. Irrigation and mineral nutrition. In *The Avocado: Botany, Production and Uses*; Whiley, A.W., Schaffer, B., Wolstenholme, B., Eds.; CABI Publishing: New York, NY, USA, 2002; pp. 259–299.
35. Lovatt, C.J. *Hass Avocado Nutrition Research in California*; University of California: Riverside, CA, USA, 2013.
36. Hapuarachchi, N.S.; Kämper, W.; Wallace, H.M.; Bai, S.H.; Ogbourne, S.M.; Nichols, J.; Trueman, S.J. Boron effects on fruit set, yield, quality and paternity of Hass avocado. *Agronomy* **2022**, *12*, 1479. [CrossRef]
37. Wu, D.; Johansen, K.; Phinn, S.; Robson, A. Suitability of airborne and terrestrial laser scanning for mapping tree crop structural metrics for improved orchard management. *Remote Sens.* **2020**, *12*, 1647. [CrossRef]
38. Subedi, P.P.; Walsh, K.B. Assessment of avocado fruit dry matter content using portable near infrared spectroscopy: Method and instrumentation optimisation. *Postharvest Biol. Technol.* **2020**, *161*, 111078. [CrossRef]
39. Mickelbart, M.; Miller, R.; Parry, S.; Arpaia, M.; Heath, R. Avocado leaf surface morphology. *Calif. Avocado Soc. Yearb.* **2000**, *84*, 139–150.
40. McGeehan, S.L.; Naylor, D.V. Automated instrumental analysis of carbon and nitrogen in plant and soil samples. *Commun. Soil Sci. Plant Anal.* **1988**, *19*, 493–505. [CrossRef]

41. Rayment, G.; Higginson, F. *Australian Laboratory Handbook of Soil and Water Chemical Methods*; Inkata Press: Melbourne, Australia, 1992.
42. Martinie, G.D.; Schilt, A.A. Investigation of the wet oxidation efficiencies of perchloric acid mixtures for various organic substances and the identities of residual matter. *Anal. Chem.* **1976**, *48*, 70–74. [CrossRef]
43. Munter, R.; Grande, R. Plant tissue and soil extract analysis by ICP-atomic emission spectrometry. In *Developments in Atomic Plasma Spectrochemical Analysis*; Byrnes, R.M., Ed.; Heyden: London, UK, 1981; pp. 653–672.
44. Tahmasbian, I.; Bai, S.H.; Wang, Y.; Boyd, S.; Zhou, J.; Esmaeilani, R.; Xu, Z. Using laboratory-based hyperspectral imaging method to determine carbon functional group distributions in decomposing forest litterfall. *Catena* **2018**, *167*, 18–27. [CrossRef]
45. Tahmasbian, I.; Xu, Z.; Abdullah, K.; Zhou, J.; Esmaeilani, R.; Nguyen, T.T.N.; Bai, S.H. The potential of hyperspectral images and partial least square regression for predicting total carbon, total nitrogen and their isotope composition in forest litterfall samples. *J. Soils Sediments* **2017**, *17*, 2091–2103. [CrossRef]
46. Rinnan, Å.; Van den Berg, F.; Engelsen, S.B. Review of the most common pre-processing techniques for near-infrared spectra. *Trends Anal. Chem.* **2009**, *28*, 1201–1222. [CrossRef]
47. Kamruzzaman, M.; Makino, Y.; Oshita, S. Parsimonius model development for real time monitoring of moisture in red meat using HSI. *Food Chem.* **2016**, *196*, 1084–1091. [CrossRef]
48. Fearn, T. On orthogonal signal correction. *Chemometr. Intell. Lab. Syst.* **2000**, *50*, 47–52. [CrossRef]
49. Wold, S.; Sjöström, M.; Eriksson, L. PLS-regression a basic tool of chemometrics. *Chemometr. Intell. Lab. Syst.* **2001**, *58*, 109–130. [CrossRef]
50. Berrueta, L.A.; Alonso-Salces, R.M.; Héberger, K. Supervised pattern recognition in food analysis. *J. Chromatogr. A* **2007**, *1158*, 196–214. [CrossRef]
51. Bellon-Maurel, V.; Fernandez-Ahumada, E.; Palagos, B.; Roger, J.M.; McBratney, A. Critical review of chemometric indicators commonly used for assessing the quality of the prediction of soil attributes by NIR spectroscopy. *Trends Anal. Chem.* **2010**, *29*, 1073–1081. [CrossRef]
52. Morellos, A.; Pantazi, X.E.; Moshou, D.; Alexandridis, T.; Whetton, R.; Tziotzios, G.; Wiebensohn, J.; Bill, R.; Mouazen, A.M. Machine learning based prediction of soil total nitrogen, organic carbon and moisture content by using VIS-NIR spectroscopy. *Biosyst. Eng.* **2016**, *152*, 104–116. [CrossRef]
53. Chang, C.W.; Laird, D.A.; Mausbach, M.J.; Hurburgh, C.R. Near-infrared reflectance spectroscopy–principal components regression analyses of soil properties. *Soil Sci. Soc. Am. J.* **2001**, *65*, 480–490. [CrossRef]
54. Camo. *The Unscrambler® X v10.3 User Manual*; Camo Software: Oslo, Norway, 2019.
55. Tamayo, Á.; Bernal, A.; Díaz, A.D.C. Composition and removal of nutrients by the harvested fruit of avocado cv. Hass in Antioquia. *Rev. Fac. Nac. Agron. Medellin.* **2018**, *71*, 8511–8516. [CrossRef]
56. Salazar-García, S.; Álvarez-Bravo, A.; Ibarra-Estrada, M.; Mellado-Vázquez, A. Accumulation of nutrients during the development of 'Méndez' avocado fruit. *Terra Latinoam.* **2019**, *37*, 469–478. [CrossRef]
57. Campisi-Pinto, S.; Zheng, Y.; Rolshausen, P.E.; Crowley, D.E.; Faber, B.; Bender, G.; Bianchi, M.; Khuong, T.; Lovatt, C.J. Optimal nutrient concentration ranges of 'Hass' avocado cauliflower stage inflorescences—Potential diagnostic tool to optimize tree nutrient status and increase yield. *HortScience* **2017**, *52*, 1707–1715. [CrossRef]
58. Farrar, M.B.; Wallace, H.M.; Tahmasbian, I.; Yule, C.M.; Dunn, P.K.; Bai, S.H. Rapid assessment of soil carbon and nutrients following application of organic amendments. *Catena* **2023**, *223*, 106928. [CrossRef]
59. Zhang, X.; Liu, F.; He, Y.; Gong, X. Detecting macronutrients content and distribution in oilseed rape leaves based on hyperspectral imaging. *Biosyst. Eng.* **2013**, *115*, 56–65. [CrossRef]
60. Melado-Herreros, A.; Nieto-Ortega, S.; Olabarrieta, I.; Gutiérrez, M.; Villar, A.; Zufía, J.; Gorretta, N.; Roger, J.M. Postharvest ripeness assessment of 'Hass' avocado based on development of a new ripening index and Vis-NIR spectroscopy. *Postharvest Biol. Technol.* **2021**, *181*, 111683. [CrossRef]
61. Maftoonazad, N.; Karimi, Y.; Ramaswamy, H.S.; Prasher, S.O. Artificial neural network modeling of hyperspectral radiometric data for quality changes associated with avocados during storage. *J. Food Process. Preserv.* **2011**, *35*, 432–446. [CrossRef]
62. Mayr, S.; Beć, K.B.; Grabska, J.; Wiedemair, V.; Pürgy, V.; Popp, M.A.; Bonn, G.K.; Huck, C.W. Challenging handheld NIR spectrometers with moisture analysis in plant matrices: Performance of PLSR vs. GPR vs. ANN modelling. *Spectrochim Acta A Mol. Biomol. Spectrosc.* **2021**, *249*, 119342. [CrossRef] [PubMed]
63. Prananto, J.A.; Minasny, B.; Weaver, T. Near infrared (NIR) spectroscopy as a rapid and cost-effective method for nutrient analysis of plant leaf tissues. In *Advances in Agronomy*; Sparks, D.L., Ed.; Academic Press: Cambridge, MA, USA, 2020; Volume 164, pp. 1–49.
64. Lassalle, G.; Fabre, S.; Credoz, A.; Hédacq, R.; Dubucq, D.; Elger, A. Mapping leaf metal content over industrial brownfields using airborne hyperspectral imaging and optimized vegetation indices. *Sci. Rep.* **2021**, *11*, 2. [CrossRef]
65. Wieczorek, D.; Żyszka-Haberecht, B.; Kafka, A.; Lipok, J. Determination of phosphorus compounds in plant tissues: From colorimetry to advanced instrumental analytical chemistry. *Plant Methods* **2022**, *18*, 22. [CrossRef] [PubMed]
66. Santoso, H.; Tani, H.; Wang, X.; Segah, H. Predicting oil palm leaf nutrient contents in Kalimantan, Indonesia by measuring reflectance with a spectroradiometer. *Int. J. Remote Sens.* **2019**, *40*, 7581–7602. [CrossRef]
67. Kuska, M.T.; Behmann, J.; Mahlein, A.K. Potential of hyperspectral imaging to detect and identify the impact of chemical warfare compounds on plant tissue. *Pure Appl. Chem.* **2018**, *90*, 1615–1624. [CrossRef]

68. Zhou, X.; Sun, J.; Tian, Y.; Lu, B.; Hang, Y.; Chen, Q. Hyperspectral technique combined with deep learning algorithm for detection of compound heavy metals in lettuce. *Food Chem.* **2020**, *321*, 126503. [CrossRef]
69. Ruffing, A.M.; Anthony, S.M.; Strickland, L.M.; Lubkin, I.; Dietz, C.R. identification of metal stresses in *Arabidopsis thaliana* using hyperspectral reflectance imaging. *Front. Plant Sci.* **2021**, *12*, 624656. [CrossRef]
70. Blanke, M.M.; Lovatt, C.J. Anatomy and transpiration of the avocado inflorescence. *Ann. Bot.* **1993**, *71*, 543–547. [CrossRef]
71. Newett, S. Little evidence to support the use of foliar applied nutrients in avocado. *Talk. Avocados* **2000**, *11*, 24–27.
72. Wolstenholme, B.N.; Whiley, A.W. Ecophysiology of the avocado (*Persea americana* Mill.) tree as a basis for pre-harvest management. *Rev. Chapingo Ser. Hortic.* **1999**, *5*, 77–88.
73. Rodriguez, E.A.G.; Penariol, M.P.; Aguiar, P.L.A.C.; Panizzi, R.C.; Andrade, R.A. Parameters for the standardization of chlorophyll and assessment of PS II quantum efficiency for avocado (*Persea americana* Mill). *Biosci. J.* **2017**, *33*, 968–978. [CrossRef]
74. Hofman, P.; Marques, R.; Searle, C.; Stubbings, B.; Moody, P. Improving avocado fruit quality through tree nutrition. In Proceedings of the New Zealand and Australia Avocado Grower's Conference, Tauranga, New Zealand, 20–22 September 2005.
75. Salazar-García, S.; Cossio-Vargas, L.E.; González-Durán, I.J.L. Correction of chronic zinc deficiency in 'Hass' avocado. *Rev. Chapingo Ser. Hortic.* **2008**, *14*, 153–159.
76. Selladurai, R.; Awachare, C.M. Nutrient management for avocado (*Persea americana* miller). *J. Plant Nutr.* **2020**, *43*, 138–147. [CrossRef]
77. Escobar, J.V.; Cortes, M.; Correa, G.; Rondon, T.; Rodríguez, P. 'Hass' avocado internal disorders under simulated export conditions and its relationship with flesh mineral content and preharvest variables. *Horticulturae* **2021**, *7*, 77. [CrossRef]